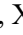



# Simulation and Evaluation of Thermal Effects Under MRI for Cochlear Implants

Yuanling Ma<sup>1</sup>, Dian Yang<sup>2</sup>, Liping Qin<sup>3</sup>, Xuesong Ye<sup>4</sup><sup>a</sup> and Congcong Zhou<sup>5</sup><sup>b</sup>

<sup>1</sup>Biosensor National Special Laboratory, Key Laboratory of Biomedical Engineering of Ministry of Education, College of Biomedical Engineering and Instrument Science, Zhejiang University, Hangzhou, 310027, China

<sup>2</sup>Zhe Jiang Key Laboratory of Intelligent Rehabilitation and Translational Neuroelectronics, China

<sup>3</sup>Zhejiang Institute of Medical Device Supervision and Testing, China

<sup>4</sup>National Engineering Research Center for Innovation And Application of Minimally Invasive Instruments, College of Biomedical Engineering and Instrument Science, Zhejiang University, Hangzhou, 310027, China

<sup>5</sup>National Engineering Research Center for Innovation And Application of Minimally Invasive Instruments, Sir Run Run Shaw Hospital, School of Medicine, Zhejiang University, China


**Keywords:** RF-Induced Heating, Finite Element Method, Cochlear, Electromagnetic Safety.


**Abstract:** Cochlear implantation is a widely used rehabilitation method for severe sensorineural deafness, but MRI scans can induce RF heating in implants, posing safety risks to patients. In this study, a novel finite-element-based electromagnetic and thermal coupled simulation method to obtain the temperature distribution and maximum temperature rise due to RF-induced heating is studied. This method allows for a quick analysis of the worst-case implant configurations and an evaluation of RF heating effects. Additionally, for cochlear implants, we propose a refined model parameters setting method which using a localized cochlear phantom in simulations to analyse key factors affecting RF-induced heating include electrode length, lead trajectory, and phantom model. In this paper, RF heating was evaluated using two phantoms, three electrode lengths, and three typical lead trajectories, with the highest temperature rise observed at 1.922°C in the cochlear phantom. The results show that small variations in electrode length have less impact compared to wire trajectory and phantom model, indicating the need for greater focus on these factors when assessing RF heating in active implants.

## 1 INTRODUCTION

Deafness is one of the most prevalent disabling conditions worldwide. The World Health Organization (WHO) estimates that hearing impairment costs the global economy approximately \$750 billion annually. Among the primary causes of deafness is severe to profound hearing impairment, which leads to disabling hearing loss (Chadha et al., 2021). For patients with severe or profound sensorineural deafness, cochlear implantation remains the only effective method of rehabilitation (Buchman et al., 2020). The increasing necessity for MRI in cochlear implant users demands rigorous safety assessments (Alberalar et al., 2023), with RF-induced heating being a pivotal area of focus.

Magnetic resonance imaging (MRI) is a widely used diagnostic tool in clinical practice due to its numerous advantages. It is non-invasive, free of ionizing radiation, and can visualize internal structures like the heart and blood vessels without the use of contrast agents. MRI also offers high-resolution imaging of soft tissues, minimal interference from bone artifacts, and multidirectional and multiparametric imaging capabilities (Koptyug et al., 2023). However, the increasing strength of MRI magnetic fields, combined with the advancement of new MRI technologies, has raised concerns regarding the biological effects and safety of MRI, particularly for patients with medical implants. The high-power radiofrequency (RF) coils used in MRI systems can induce electromagnetic resonance in conductive implants, leading to RF-induced heating, which may

<sup>a</sup> <https://orcid.org/0000-0002-3439-3733>

<sup>b</sup> <https://orcid.org/0000-0001-8397-1491>

cause irreversible tissue damage, such as burns. This is especially concerning for patients with implants located near sensitive areas, like the brain(Rezai et al., 2002). Cochlear implants, positioned subcutaneously behind the ear and close to the brain, are particularly susceptible to this risk, making RF-induced heating a critical safety issue that requires thorough testing.

Previous studies primarily focused on in vivo testing, a method involving the implantation of devices into animals or human subjects, followed by the monitoring of physiological parameters in an MRI environment. Crane et al. conducted a retrospective analysis of the safety and diagnostic validity of cochlear implants in patients undergoing MRI scans(Crane et al., 2010). However, their study was limited by the absence of quantitative measurements and a lengthy experimental timeline. Additionally, Luechinger et al. evaluated the RF safety of cochlear implants in experimental pigs (Long White breed), while Roger et al. assessed the radiofrequency safety of pacemaker leads in Danish Long White pigs(Luechinger et al., 2005). Despite these efforts, the in vivo approach was constrained by the limitations of measuring locations and difficulties in obtaining precise data.

To ensure standardization, avoid potential medical ethical issues, and improve experimental convenience, the ASTM F2182 standard outlines a test procedure in which the implant is embedded in a gelatinized saline-filled body phantom, exposed to an RF field with a whole-body average specific absorption rate (SAR) of 2 W/kg using a benchtop system. The temperature is monitored for 15 minutes, and the local SAR is determined using a calorimetric method(ASTM\_International, 2019). Yang et al. found that, for devices implanted in or near bone tissue, the assessment of RF-EMF energy deposition using an ASTM model that incorporates bone provided a better correlation with human models compared to the standard ASTM model(Yang et al., 2024). However, despite the widespread use and study of in vitro body models for RF heating evaluations, significant limitations remain. The human body is a complex, heterogeneous environment composed of various tissues, and the homogeneous gel-saline models used cannot sufficiently mimic the diverse properties of human tissues to accurately reflect the heating effects of implants in such a complex biological environment(Ran et al., 2017).

The ISO/TS 10974:2018 standard outlines a four-layer test methodology designed to account for the wide range of configurations and applications of active implantable medical devices (AIMDs), aiming

to provide a conservative estimate of energy deposition in controlled in vitro test systems (Standardization, 2018). Numerous studies have also employed the Finite-Difference Time-Domain (FDTD) method and transfer function approach to assess RF-induced heating. For example, Zeng et al. evaluated RF heating in a cochlear implant within a 1.5T MRI coil using the FDTD method, alongside a virtual human body model for electromagnetic simulation, and employed the transfer function approach to estimate temperature rise. They also explored variables such as lead type, trajectory, and MRI parameters on RF heating effects(Zeng et al., 2018). Similarly, Islam et al. investigated RF-induced heating in partially inserted electrodes in 1.5T MRI systems, revealing that heating was significantly influenced by factors such as contact size, spacing, lead length, and clinically relevant trajectories(Islam et al., 2023). While this approach has become widely adopted due to its ability to maintain the complexity of the implant system's microstructure, it has some limitations. The accuracy of FDTD EM simulations is moderate, and the measurement of transfer functions requires physical prototypes, making repeated testing time-consuming and less suitable for implants with complex and variable wire geometries, such as cochlear implants. In such cases, alternative methodologies may offer better efficiency and precision(Winter et al., 2021).

The assessment of RF-EMF safety requires consideration of curved components such as birdcage coils and implant electrodes. In this context, the Finite Element Method (FEM) emerges as an optimal approach, offering enhanced precision in analyzing complex, curved geometries compared to other techniques(Winter et al., 2021). This paper introduces a combined electromagnetic and temperature field simulation method, based on the FEM approach, to evaluate RF-EMF-induced heating in a cochlear implant system within a 1.5T MRI coil. The method facilitates the assessment of heating effects on the cochlear implant system and investigates the key factors influencing these thermal effects.

## 2 MATERIALS AND METHODS

### 2.1 Cochlear Implants

The contemporary generation of cochlear implants consists of two principal components: the implant and an external sound processor. The electrode array in modern cochlear implants typically contains 12 to 22 electrodes, although the exact number may vary

depending on device design and specific clinical requirements. This array, approximately 2 cm in length, is connected to one or more internal current sources, which are activated based on commands from the external device (Macherey & Carlyon, 2014). The external sound processor, worn behind the ear, is removable and can be detached during magnetic resonance imaging (MRI) examinations. As a result, this study focuses exclusively on the radiofrequency electromagnetic field RF-induced heating of the implant portion.

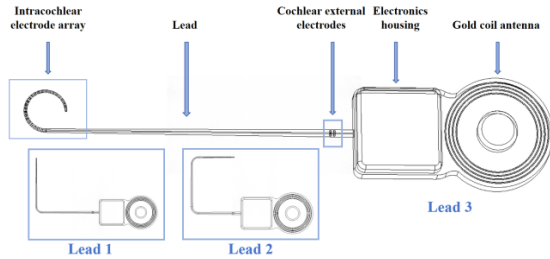


Figure 1: Representative configurations of cochlear implant.

As illustrated in Figure 1, a typical cochlear implant designed by Nurotron comprises consists of several key components, including the intracochlear electrode array, lead, extracochlear electrodes, electronic housing, and gold coil antenna. The intracochlear electrode array is depicted as a 24-electrode cylinder with radii of 0.4 mm, 0.5 mm, and 0.6 mm, respectively, tapering towards the tip of the lead. To accommodate the anatomical variation of the patient's cochlea and case-specific requirements, the length of the electrode array can be selected from 17.5 mm, 22.0 mm, or 25.5 mm. Additionally, two extracochlear electrodes are also implemented in the system.

## 2.2 Phantom for Cochlear Implants

The ASTM phantom was used in place of the human body for the simulation. Since the cochlear implant is typically implanted in the human cochlea, and the main components of the cochlear environment include the cochlear canal as well as internal and external lymphatic fluids (Fatani et al., 2024), a configuration simulating the cochlear environment was incorporated. The specific parameters of this configuration are presented in Table 1 (Hasgall PA, 2024), where  $\epsilon_r$  is the relative dielectric constant,  $\sigma$  (unit: S/m) is the conductivity,  $k$  (unit: W/(m<sup>2</sup>·K)) is the coefficient of thermal

conductivity,  $c$  (unit: J/(kg·K)) is the heat capacity,  $\rho$  (unit: kg/m<sup>3</sup>) is the density.

Table 1: Material parameters.

Phantom	$\epsilon_r$	$\sigma$	$k$	$c$	$\rho$
ASTM phantom	80	0.47	0.57	4150	1050
Cochlear phantom	57.75	0.32	0.46	3226	1089

The location and trajectory of the cochlear implant within the ASTM phantom are illustrated in Figure 2. The implant is positioned at the center of the ASTM phantom, 45 mm from both the top and bottom of the gel, aligned with the aperture direction, and 2 cm from the sidewalls, where a relatively high and evenly distributed electric field exists. Given that RF-induced heating of partially inserted electrodes is closely correlated with clinically relevant trajectories (Islam et al., 2023), and cochlear implantation often involves electrode bending, this paper discusses several typical simplified cochlear bending trajectories.

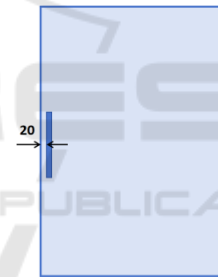


Figure 2: The position and dimension of inserted bone structure. Unit: mm.

## 2.3 Coupled EM and Thermal Simulations

An 8-rung 1.5T low-pass birdcage coil (diameter: 800 mm, length: 700 mm) was used to generate a circularly polarized electromagnetic field, driven in quadrature mode at 64 MHz. The ASTM phantom with the implant was positioned such that the center of the phantom aligned with the isocenter of the RF coil. To ensure proper electromagnetic isolation and stable tuning, an RF shield was integrated around the exterior of the birdcage coil. Scattering boundary conditions were applied to truncate the computational region, effectively simulating real-world conditions. The initial value of the capacitance was estimated using the Birdcage Builder Software developed by Penn State University (Chin et al., 2002). A subsequent scanning search was conducted in the

vicinity of this value to determine the optimal capacitance, which was approximately 12.3 pF.

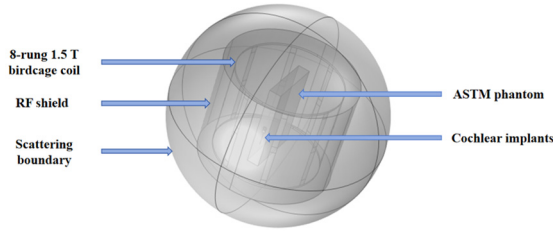


Figure 3: Illustration of simulation setup, the position of various components.

A sequential coupled electromagnetic and thermal analysis was performed using the Finite Element Method (FEM) simulation software COMSOL Multiphysics to calculate the electric and temperature fields for the ASTM phantom cochlear implant model. Maxwell's equations were employed to solve the fluctuating electromagnetic fields at specific points within the model, influenced by the electromagnetic field under investigation, in the steady-state frequency domain. The steady-state electromagnetic solution of Maxwell's equations provided the heat source for the transient thermal analysis, which yielded the electromagnetic solution for all domains and the heat transfer solution within the ASTM body model and the implant. Using the SAR as the heat source for the temperature rise, the temperature field distribution within the model is obtained by solving the heat conduction equation through the Finite Element Method (FEM), as shown in Eq. (1), where  $\rho$  is the density of the phantom,  $c$  is the specific heat capacity of the phantom,  $k$  is the thermal diffusivity,  $T$  is the temperature at a point in space,  $t$  is time and  $Q$  is the heat source.

$$\rho c \frac{\partial T}{\partial t} = k \nabla^2 T + Q = k \nabla^2 T + SAR \quad (1)$$

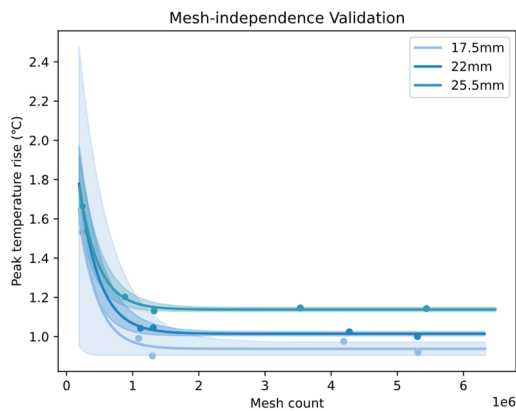


Figure 4: Illustration of mesh-independence validation.

A non-uniform mesh was utilized in the simulation, with the mesh density near critical inflection points selected as the final simulation mesh based on mesh-independence validation. This approach reduced computational costs while maintaining accurate modelling.

### 3 RESULTS AND DISCUSSION

All results were obtained through numerical simulations using the methodology described above, with the input power of RF coil normalized to a whole-body average SAR of 2 W/kg, in accordance with the IEC 60601-2-33 power limitation criterion for the MR normal mode of operation (Commission, 2022). This study evaluates RF-induced heating in two phantoms with three different electrode lengths and three typical simplified cochlear implant bending trajectory scenarios. This study will analyze the RF-induced heating by examining the spatial and temporal distribution and variation of temperature. It will focus on potential factors affecting maximum temperature rise, including electrode length, lead trajectory, and phantom models.

Table 2: Statistical analysis of temperature rises in phantom around the lead tip under all the studied exposure conditions. (Unit: °C)

(a) ASTM phantom			
Bending trajectories	17.5mm electrode length	22mm electrode length	25.5mm electrode length
Lead 1	1.458	1.459	1.461
Lead 2	1.589	1.629	1.746
Lead 3	1.592	1.592	1.597

(b) cochlear phantom			
Bending trajectories	17.5mm electrode length	22mm electrode length	25.5mm electrode length
Lead 1	1.456	1.479	1.518
Lead 2	1.736	1.793	1.898
Lead 3	1.906	1.921	1.922

The statistical results of all simulations are presented in Table 2. In the ASTM phantom, the maximum temperature rises for Lead 1, Lead 2, and Lead 3 were 1.461°C, 1.746°C, and 1.594°C, respectively. A similar trend was observed in the cochlear model, where the maximum temperature rises were 1.518°C, 1.898°C, and 1.956°C for Lead 1, Lead 2, and Lead 3, respectively. For a given trajectory, the maximum temperature rise was

consistently higher in the cochlear phantom compared to the ASTM phantom.

### 3.1 Temperature Rise Distribution

By analyzing the spatial distribution of temperature rise, based on the model's exposure to RF electromagnetic fields for 15 minutes, as shown in Fig. 5, it can be concluded that in several scenarios examined in this study, the areas with the highest temperature increases are concentrated at the ends of the gold coil, the outer cochlear electrode, and the tip of the inner cochlear electrode. The hotspot is primarily located at the tip of the inner cochlear electrode, which warrants focused attention in further research. Theoretically, the implant can be considered an RF antenna that captures energy along its length and dissipates the maximum energy density near its end (Pozar, 2021), which aligns with the observed hotspot at the tip of the intracochlear electrode.

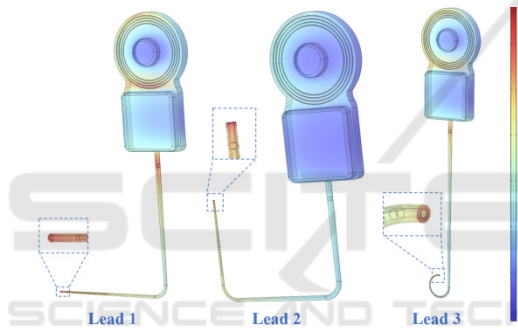


Figure 5: Distribution of temperature rise around the implant after 15 minutes of exposure.

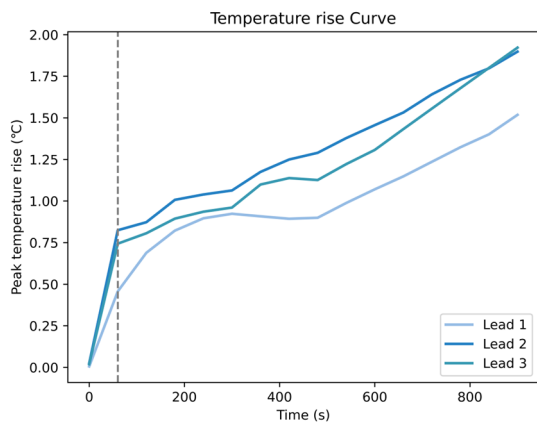


Figure 6: Temperature rise curves for the maximum temperature rise case for three bending trajectories.

In the time domain, the temperature rise curve shown in Fig. 6 exhibits a rapid, near-linear increase, followed by a gradual leveling off. The rate of

temperature change over time depends on the balance between the power density absorbed from the RF source and heat conduction within the phantom material. As the temperature rise becomes significant, heat conduction begins transferring heat from the implant to the surrounding material, which slows the rate of further temperature increase.

### 3.2 Electrode Length

Temperature rises were calculated for three electrode lengths in both ASTM and cochlear phantoms to investigate the effect of electrode length on RF-induced heating. The electrode lengths, chosen based on recommendations from implant surgeons, were 17.5 mm, 22.0 mm, and 25.5 mm to accommodate different cochlear anatomical structures and case variations. The type and number of electrodes remained consistent across lengths, with the primary difference being the spacing between electrodes. The mean RF-induced temperature rises for electrode lengths of 17.5 mm, 22.0 mm, and 25.5 mm were 1.546°C, 1.560°C, and 1.600°C in the ASTM phantom, and 1.699°C, 1.743°C, and 1.779°C in the cochlear phantom. As illustrated in Figure 7(a), the maximum temperature rise tended to increase with longer electrode lengths in both phantoms.

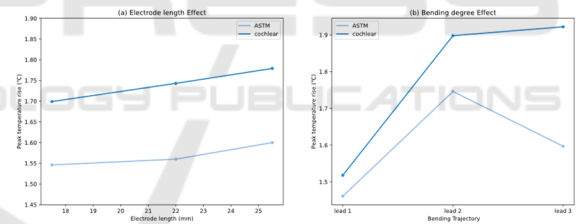


Figure 7: (a) Line graph showing the average maximum temperature rise for different electrode lengths in both the ASTM and cochlear phantoms, (b) line graph showing the maximum temperature rise for different bending trajectories in both the ASTM and cochlear phantoms.

When the implant's size is approximately half the wavelength, a significant temperature rise occurs due to the resonance effect (Konings et al., 2000). This resonance phenomenon is heavily influenced by the electrical properties and the operating frequency of the medium surrounding the implant. Neglecting magnetic permeability, the wavelength of an electromagnetic wave  $\lambda_m$  in a given material can be calculated using Eq. (2), where  $\lambda_0$  is the wavelength of the electromagnetic wave in vacuum and  $\epsilon_r$  is the relative dielectric constant.

$$\lambda_m = \frac{\lambda_0}{\sqrt{\epsilon_r}} \quad (2)$$



The wavelength of an electromagnetic wave in a vacuum  $\lambda_0$  is related to the RF frequency. In this study, the research focuses on the 1.5T case. According to Eq. (3), the wavelength can be calculated as approximately 4.6875m.

$$\lambda_0 = \frac{c}{f} \quad (3)$$

The relative permittivity of the ASTM phantom is 80, while that of the cochlear phantom is 57.75. Using these values and applying Eq. (2), the theoretical half-wavelengths are calculated as 26.20 and 30.84mm, respectively, for ASTM and cochlear phantom. The cochlear implant leads tested thus far have not reached this length, so, theoretically, the temperature rise is expected to increase as the lead length increases. The conclusion that the maximum temperature rise increases with longer electrode length aligns with theoretical expectations.

### 3.3 Bending Trajectory

Cochlear implantation often involves lead bending, and three typical simplified bending trajectories, as shown in Fig. 1, were investigated for both the ASTM and cochlear phantoms. Figure 7(b) illustrates the surrounding temperature rise for different implantation trajectories in the two phantoms, with maximum temperature rises of 1.518°C, 1.898°C, and 1.922°C for trajectories 1, 2, and 3, respectively. It can be tentatively estimated that trajectories with a greater degree of curvature and a smaller bending range will concentrate more heat and cause a larger temperature rise.

### 3.4 Phantom Model

The RF-induced thermogenesis of the same implant differs between the ASTM and cochlear phantoms. Table 2 and Figure 7 presents histograms of the maximum temperature rise in both phantoms, showing that the mean maximum temperature rise in the ASTM phantom is 1.569°C, which is lower than the 1.737°C observed in the cochlear phantom. In all cases, the maximum temperature rise in the ASTM phantom is lower than that in the cochlear phantom. Similar to Yang et al.'s study, relying solely on the ASTM phantom for localized areas may result in temperature rise deviations (Yang et al., 2024). In this paper, it is shown as an underestimation of the maximum temperature rise. Therefore, when assessing the RF thermogenic safety of cochlear implants more localized scenarios should be considered.

## 4 CONCLUSIONS

In this study, we introduce a model that simulates the cochlear environment to improve the assessment of RF-induced heating near cochlear implants. This model provides results that more accurately reflect the intracochlear conditions compared to the ASTM model, verifying that the ASTM model may have underestimated the maximum temperature rise. Additionally, we propose a finite element-based electromagnetic and thermal co-simulation method to obtain the temperature distribution and maximum temperature rise from RF thermogenesis. This approach enables rapid analysis of worst-case implant configurations and predicts RF thermogenesis outcomes, helping to guide future experiments and implant design. Using this method, we examine factors such as electrode length and wire trajectory, highlighting the importance of focusing on the hotspot at the tip of the electrode and emphasizing the need to control electrode length where possible.

## ACKNOWLEDGEMENTS

This research was supported by the Key Research and Development Plan of Zhejiang Province (Grant Nos. 2023C03094) and Zhejiang Provincial Natural Science Foundation of China under Grant No. LY22H180006.

## REFERENCES

- Alberalar, N. D., Reis, J., Piechotta, P. L., Beetz, N. L., Fehrenbach, U., Geisel, D., Thomas, A., Busse, H., & Denecke, T. (2023). Complications of cochlear implants with MRI scans in different body regions: type, frequency and impact. *Insights into imaging*, 14(1), 9. <https://doi.org/10.1186/s13244-022-01353-x>
- ASTM International. (2019). Standard Test Method for Measurement of Radio Frequency Induced Heating On or Near Passive Implants During Magnetic Resonance Imaging(F2182 - 19e2).
- Buchman, C. A., Gifford, R. H., Haynes, D. S., Lenarz, T., O'Donoghue, G., . . . Zwolan, T. (2020). Unilateral Cochlear Implants for Severe, Profound, or Moderate Sloping to Profound Bilateral Sensorineural Hearing Loss: A Systematic Review and Consensus Statements. *JAMA Otolaryngol Head Neck Surg*, 146(10), 942-953. <https://doi.org/10.1001/jamaoto.2020.0998>
- Chadha, S., Kamenov, K., & Cieza, A. (2021). The world report on hearing, 2021. *Bull World Health Organ*, 99(4), 242-242a. <https://doi.org/10.2471/blt.21.285643>

- Chin, C. L., Collins, C. M., Li, S., Dardzinski, B. J., & Smith, M. B. (2002). BirdcageBuilder: Design of Specified-Geometry Birdcage Coils with Desired Current Pattern and Resonant Frequency. *Concepts Magn Reson*, 15(2), 156-163. <https://doi.org/10.1002/cmr.10030>
- Commission, I. E. (2022). Particular requirements for the basic safety and essential performance of magnetic resonance equipment for medical diagnosis.(IEC 60601-2-33 ED4.0).
- Crane, B. T., Gottschalk, B., Kraut, M., Aygun, N., & Niparko, J. K. (2010). Magnetic resonance imaging at 1.5 T after cochlear implantation. *Otol Neurotol*, 31(8), 1215-1220. <https://doi.org/10.1097/MAO.0b013e3181ec1d61>
- Fatani, N., Abdelsamad, Y., & Alsanosi, A. (2024). Influence of Cochlear Anatomy on Intraoperative Electrically Evoked Compound Action Potentials. *J Clin Med*, 13(16). <https://doi.org/10.3390/jcm13164716>
- Hasgall PA, D. G. F., Baumgartner C, Neufeld E, Lloyd B, Gosselin MC, Payne D, Kligenböck A and Kuster N. (2024). *IT'IS Database for Thermal and Electromagnetic Parameters of Biological Tissues, Version 4.2*. <https://doi.org/10.13099/VIP21000-04-2>.
- Islam, M. Z., Hu, W., Guo, R., & Chen, J. (2023). *Factors Affecting the RF-Induced Heating for the Electrodes Partially Inserted Inside Human Body at 1.5T MRI* 2023 IEEE International Symposium on Antennas and Propagation and USNC-URSI Radio Science Meeting (USNC-URSI).
- Konings, M. K., Bartels, L. W., Smits, H. F., & Bakker, C. J. (2000). Heating around intravascular guidewires by resonating RF waves. *Journal of Magnetic Resonance Imaging*, 12(1), 79-85.
- Koptyug, I., Kovtunov, K., & Svyatova, A. (2023). Magnetic Resonance Imaging (MRI). In I. E. Wachs & M. A. Bañares (Eds.), *Springer Handbook of Advanced Catalyst Characterization* (pp. 849-867). Springer International Publishing. [https://doi.org/10.1007/978-3-031-07125-6\\_37](https://doi.org/10.1007/978-3-031-07125-6_37)
- Luechinger, R., Zeijlemaker, V. A., Pedersen, E. M., Mortensen, P., Falk, E., . . . Boesiger, P. (2005). In vivo heating of pacemaker leads during magnetic resonance imaging. *Eur Heart J*, 26(4), 376-383; discussion 325-377. <https://doi.org/10.1093/eurheartj/ehi009>
- Macherey, O., & Carlyon, R. P. (2014). Cochlear implants. *Current Biology*, 24(18), R878-R884. <https://doi.org/10.1016/j.cub.2014.06.053>
- Pozar, D. M. (2021). *Microwave engineering: theory and techniques*. John Wiley & sons.
- Ran, G., Jianfeng, Z., & Ji, C. (2017). MRI RF-Induced Heating in Heterogeneous Human Body with Implantable Medical Device. In H. Ahmet Mesrur (Ed.), *High-Resolution Neuroimaging*. IntechOpen. <https://doi.org/10.5772/intechopen.71384>
- Rezai, A. R., Finelli, D., Nyenhuis, J. A., Hrdlicka, G., Tkach, J., . . . Shellok, F. G. (2002). Neurostimulation systems for deep brain stimulation: in vitro evaluation of magnetic resonance imaging-related heating at 1.5 tesla. *J Magn Reson Imaging*, 15(3), 241-250. <https://doi.org/10.1002/jmri.10069>
- Standardization, I. O. f. (2018). Assessment of the safety of magnetic resonance imaging for patients with an active implantable medical device(Tech Specif ISOTS 10974 2018, second edition).
- Winter, L., Seifert, F., Zilberti, L., Murbach, M., & Ittermann, B. (2021). MRI-Related Heating of Implants and Devices: A Review. *J Magn Reson Imaging*, 53(6), 1646-1665. <https://doi.org/10.1002/jmri.27194>
- Yang, X., Guo, R., Zheng, J., Long, S. A., Chen, X., & Chen, J. (2024). Improved assessment of radiofrequency electromagnetic field power deposition near orthopaedic device using a bone-inclusive ASTM phantom under 1.5 T and 3T MRI. *Physics in Medicine & Biology*, 69(16), 165024.
- Zeng, Q., Wang, Q., Zheng, J., Kainz, W., & Chen, J. (2018). Evaluation of MRI RF electromagnetic field induced heating near leads of cochlear implants. *Phys Med Biol*, 63(13), 135020. <https://doi.org/10.1088/1361-6560/aacbf2>